



Universiteit  
Leiden  
The Netherlands

## Hunting dark matter with X-rays

Franse, J.

### Citation

Franse, J. (2016, December 20). *Hunting dark matter with X-rays. Casimir PhD Series*. Retrieved from <https://hdl.handle.net/1887/45082>

Version: Not Applicable (or Unknown)

License: [Licence agreement concerning inclusion of doctoral thesis in the Institutional Repository of the University of Leiden](#)

Downloaded from: <https://hdl.handle.net/1887/45082>

**Note:** To cite this publication please use the final published version (if applicable).

Cover Page



Universiteit Leiden



The handle <http://hdl.handle.net/1887/45082> holds various files of this Leiden University dissertation.

**Author:** Franse, J.

**Title:** Hunting dark matter with X-rays

**Issue Date:** 2016-12-20

---

# 4 | PERSEUS OUT TO $R_{200}$ WITH SUZAKU

---

BASED ON

*Radial Profile of the 3.55 keV line out to  $R_{200}$  in the Perseus Cluster*

Jeroen Franse, Esra Bulbul, Adam Foster, Alexey Boyarsky, Maxim Markevitch, Mark Bautz, Dmytro Iakubovskiy, Mike Loewenstein, Michael McDonald, Eric Miller, Scott W. Randall, Oleg Ruchayskiy, Randall K. Smith

Published in *The Astrophysical Journal*

## 4.1 Introduction

The recent discovery of the unidentified X-ray line at  $\sim 3.5$  keV in the stacked *XMM-Newton* and *Chandra* observations of 73 galaxy clusters and in M31 and its possible interpretation as a decaying dark matter have attracted great attention from the community (Bulbul et al. (2014a); Boyarsky et al. (2014a), Bu14 and Bo14 respectively from here on). The signal is significantly detected in the center of Perseus (the X-ray brightest cluster on the sky) by the *XMM-Newton* and *Chandra* satellites (and later confirmed with *Suzaku*; see Urban et al., 2015) and in its outskirts with *XMM-Newton* (Bo14). The signal is also observed in the Galactic Center (Boyarsky et al., 2015; Jeltema & Profumo, 2015).

Although there has been an extensive effort in the community, the origin of the line is still quite uncertain. Among the three possible interpretations of the line are an instrumental feature, an astrophysical line (e.g., from the intracluster plasma), and emission from dark matter decay or annihilation processes. An instrumental line or calibration errors as possible origins of the 3.5 keV line are extensively studied in the original discovery papers by Bu14 and Bo14. Bu14's analysis, in particular, argues that stacking blue-shifted spectra of a large sample of galaxy clusters with a wide redshift range excludes the instrumental artifact. The detection of the line by several detectors on board of *Chandra*, *XMM-Newton*, and *Suzaku* indicates that it is unlikely due to an instrumental artifact. Furthermore, non-detections in deep exposures of 'blank-sky' background observations with *XMM-Newton* and *Suzaku* also exclude an instrumental artifact (Bo14; Sekiya et al., 2015).

Another possible interpretation of the  $\sim 3.5$  keV line is spectral confusion with one

of a number of nearby weak astrophysical lines of K XVIII, Cl XVII, and Ar XVII, or possible lines from charge exchange in the intra-cluster medium. This has been extensively discussed in Bu14. Atomic transitions, specifically from the K XVIII and Ar XVII ions are hard to unambiguously distinguish from the 3.5 keV line due to the instruments' spectral resolution (CCD resolution is 100–120 eV FWHM at this energy). Bu14 report that abundances of a 10–20 times solar are required to explain the 3.5 keV excess with any of these lines based on the estimates obtained from the observed S and Ca line ratios. Jeltema & Profumo (2014, 2015) and Carlson et al. (2015) argue that an atomic transition from K XVIII in cool  $<1$  keV plasma is likely to be responsible for the 3.5 keV line. In a comment to these studies, Bulbul et al. (2014b) showed that the observed line ratios are inconsistent with the existence of any significant quantities of cool gas in clusters used in the Bu14 sample. We address further issues with the updated paper by Jeltema & Profumo (2015) and Carlson et al. (2015) in Appendix 6.3. A recent study by (Gu et al., 2015) suggests an alternative explanation for the line, i.e. charge exchange with bare sulfur ions at 3.48 keV. This interpretation is discussed in Appendix 6.1.

A more exotic explanation of the 3.5 keV line is emission from decaying dark matter (Bu14; Bo14; Boyarsky et al. (2014a); Boyarsky et al. (2014b)). Although the line intensity in the Perseus cluster core appears to be five times brighter than the flux in the stacked clusters if one scales the predicted fluxes with cluster mass as expected for dark matter decay (see Bu14), the relative intensities between other objects (M31, Galactic Center, clusters), and the surface brightness distribution within the Perseus cluster (from *XMM-Newton* measurements outside the core) are consistent with a decaying dark matter feature (Boyarsky et al., 2014a; Boyarsky et al., 2015). The detection in the Galactic center is consistent with the decaying dark matter interpretation, although this result does not exclude K XVIII as a possible origin (Boyarsky et al., 2015). The upper limits derived from the blank-sky observations (since these contain dark matter in the field of view from the Galaxy's dark matter halo) are consistent with the fluxes reported by previous studies. On the other hand, non-detections in several other studies, for instance, in stacked galaxies (Anderson et al., 2015) and in dwarf galaxies (Malyshev et al., 2014) challenge the decaying dark matter interpretation of the line. However, the reported statistical tensions across these objects are mild, at a level of  $2\text{--}3\sigma$  (with the exception of the stacked galaxies). Recently, Ruchayskiy et al. (2015) reported on the analysis of newly obtained very-long-exposure *XMM-Newton* data of the Draco satellite galaxy. A small hint of  $\sim 3.5$  keV emission was identified although the authors conservatively focus on the upper limits and determine that it is consistent with a decaying dark matter origin based on the dark matter content of the object. In another work regarding the same Draco data, Jeltema & Profumo (2016) claim a much stronger limit on the possible  $\sim 3.5$  keV line flux that is at odds with a dark matter decay interpretation. Ruchayskiy et al. (2015) suggests mainly that their more thorough spectral modeling provides a more accurate continuum model. Primary differences include additional physically motivated model components and a wider spectral fitting range (Iakubovskiy et al. (in prep.) offers a quantitative description of this effect). This influences the line flux limits and brings them in agreement with the previous detections of the 3.5 keV line. Most recently, Bulbul et al. (2016a) reported a weak spectral excess around 3.5 keV in the stacked *Suzaku* observations of 47 galaxy clusters. The upper limits derived from their analysis are consistent with the detection from the stacked clusters. However, their sample excludes the Perseus cluster which is in tension

with the previously reported line flux observed with *XMM-Newton*.

In this work we take a further step to examine the spatial distribution of the 3.5 keV line within the Perseus cluster from its core to outskirts with *Suzaku*. The 3.5 keV line is detected in the observations of the core of the Perseus cluster in both the central 6' and in the surrounding area within *Suzaku*'s field-of-view by Urban et al. (2015). The authors confirm the finding of Bu14 that the flux of the 3.5 keV line in the core is too strong for a decaying dark matter interpretation that assumes a single spherical dark matter distribution for the cluster (as measured by Simionescu et al. (2011)). Urban et al. (2015) also studied 3 other clusters observed with *Suzaku*, and did not detect any 3.5 keV line flux in them. These non-detections are consistent with the previous results for other clusters and samples (Bu14; Bo14; Boyarsky et al., 2015). We note that Tamura et al. (2015) also studied the same *Suzaku* observations of Perseus, but do not find evidence of excess emission around 3.5 keV; the origin of this discrepancy is unclear and we will discuss it below.

We here present the analysis of additional *Suzaku* data that extend the previous studies to greater radii. This paper is organized as follows: in Section 4.2, we describe the *Suzaku* data reduction and analysis. In Section 4.3, we provide our results in the cluster center and in the outskirts. We discuss systematic errors that are relevant to the *Suzaku* X-ray measurements at large radii in Section 4.2.1. In Sections 4.4 and 4.5 we discuss our results and present our conclusions. Throughout the paper, a standard  $\Lambda$ CDM cosmology with  $H_0 = 70 \text{ km s}^{-1} \text{ Mpc}^{-1}$ ,  $\Omega_\Lambda = 0.7$ , and  $\Omega_M = 0.3$  is assumed. In this cosmology, 1' at the distance of the cluster corresponds to  $\sim 21.2 \text{ kpc}$ . Unless otherwise stated, reported errors correspond to 68% (90%) confidence intervals.

## 4.2 Data Reduction and Analysis

The Perseus cluster has been observed with *Suzaku* between 2006 and 2015 for a total 2.3 Ms. We process the *Suzaku* data with HEASOFT version 6.13, and the latest calibration database CALDB as of May 2014. The raw event files are filtered using the FTOOL *aepipeline*. The detailed steps of the data processing and filtering are given in Bulbul et al. (2016b). The *Suzaku* observations utilized in this work and net exposure times of each pointing after filtering are given in Table 4.8.

Point sources in the FOV are detected from the *Suzaku* data using CIAO's *wavdetect* tool. The detection is performed using *Suzaku*'s half-power radius of 1' as the wavelet radius as described in (Urban et al., 2015). The detected point sources are excluded from further analysis. Spectra are extracted from the filtered event files in *XSELECT*. Corresponding detector redistribution function (RMF) and ancillary response function (ARF) files are constructed using the *xisrmfgen* and *xisarfgen* tools. The Night-Earth background spectra are generated using the *xisnxbgen* tool and subtracted from each total spectrum prior to fitting.

We co-add front-illuminated (FI) XIS0 and XIS3 data to simplify spectral fitting using FTOOL *mathpha*. The back-illuminated (BI) XIS1 data are co-added separately. The exposure-weighted and normalized ARFs and RMFs are stacked using the FTOOLS *ad-darf* and *addrmf*. The NXB subtracted FI and BI observations are modeled simultaneously in the 1.95 to 6 keV energy band. Following the same approach of Bu14, we model

Region Name	inner $d$ arcmin	outer $d$ arcmin	inner $d$ kpc	outer $d$ kpc
Region 1	0	8.3	0	182
Region 1a	0	2	0	44
Region 1b	2	4.5	44	98
Region 1c	4.5	8.3	98	182
Region 2	8.3	25	182	545
Region 3	25	40	545	873
Region 4	40	130	873	2836
Region 2-4	8.3	130	182	2836

**Table 4.1:** Definitions of the used spectral extraction regions in arcmin and kpc from the cluster center. ‘Region 2-4’ is the combination of Regions 2 through 4 (the full off-center dataset).

the FI and BI observations with the line-free multi-temperature *apec* models and additional Gaussian models for all the relevant atomic transitions, to allow maximum modeling freedom within physical reason. The free parameters of the model are tied between the FI and BI observations. XSPEC v12.9 is used to perform the spectral fits with the ATOMDB version 2.0.2 (Foster et al., 2012). The galactic column density is frozen at the Leiden/Argentine/Bonn (LAB) Galactic HI Survey (Kalberla et al., 2005) value of  $1.36 \times 10^{20} \text{ cm}^{-2}$  in our fits. Two wide instrumental Au M edges are modeled with two *gabs* components at 2.3 and 3.08 keV following Tamura et al. (2015).

The contribution of the soft local X-ray background (including local hot bubble and galactic halo) is negligible in our fitting band (1.95 – 6 keV), while the contribution of the cosmic X-ray background (CXB) may still be significant. To account for the contribution of CXB we add a power-law component to the model. The normalization of the power-law model is left free, while the index is fixed to 1.41 in our fits. We check for possible systematic effects regarding the CXB in Section 4.2.1.

The atomic lines and their rest-frame energies included in our model are (see also Table 4.2): Al XIII (2.05 keV), Si XIV (2.01 keV, 2.37 keV, and 2.51 keV), Si XIII (2.18 keV, 2.29 keV, and 2.34 keV), S XV (2.46 keV, 2.88 keV, 3.03 keV), S XVI (2.62 keV), Ar XVII (triplet at 3.12 keV, 3.62 keV, 3.68 keV), Cl XVI (2.79 keV), Cl XVII (2.96 keV), Cl XVIII (3.51 keV) K XVIII (triplet 3.47 keV, 3.49 keV and 3.51 keV), K XIX (3.71 keV), Ca XIX (complex at 3.86 keV, 3.90 keV, 4.58 keV), Ar XVIII (3.31 keV, 3.93 keV), Ca XX (4.10 keV), Cr XXIII (5.69 keV). After the first iteration the  $\chi^2$  improvement for the inclusion of each of these lines is determined, and lines that do not improve the fit by more than a  $\Delta\chi^2$  of 2 are removed from the model (on a region-by-region basis).

It is crucial to determine the fluxes of S XV at 2.46 keV and S XVI at 2.62 keV accurately for temperature estimation, as this line ratio is a very sensitive temperature diagnostic, especially valuable for detecting the presence of cool gas. However, the band where S XV and S XVI are located, is crowded with strong Si XIV lines. We therefore tie the fluxes of Si XIV (2.01 keV: 2.37 keV: 2.51 keV) to each other with flux ratios of (21:3.5:1). We also tie S XV (2.46 keV : 2.88 keV) lines with a flux ratio of (9:1). These ratios are based on the theoretical predictions for the typical temperatures we measure.

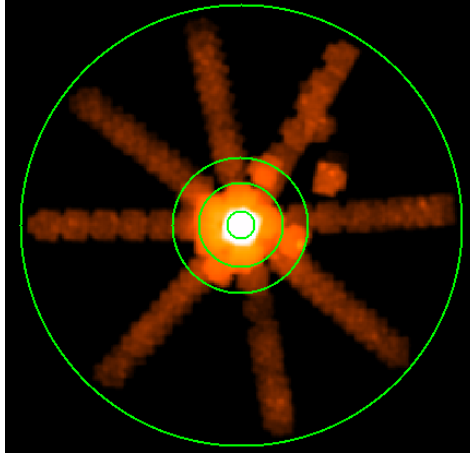


**Figure 4.1:** Countmap of all pointings used in the present analysis, with radial extraction regions shown at 8.3', 25', 40' and 130'.

Ion	E keV	Ion	E keV
Al XIII	2.05	Cl XVII	3.51
Si XIV	2.01, 2.37, 2.51	K XVIII	3.47, 3.49, 3.51
Si XIII	2.18, 2.29, 2.34	K XIX	3.71
S XV	2.46, 2.88, 3.03	Ca XIX	3.86, 3.90, 4.58
S XVI	2.62, 3.28	Ar XVIII	3.31, 3.93
Ar XVII	3.12, 3.62, 3.68	Ca XX	4.10
Cl XVI	2.79	CrXXIII	5.69
Cl XVII	2.96		

**Table 4.2:** List of atomic lines and their rest-frame energies included in the model.

The observed fluxes of some of the strong atomic lines in our fitting band are given in Table 4.4.

To model the fluxes of the K XVIII, Cl XVII, and Ar XVII lines nearest to the 3.5 keV energy in question, we use temperature estimates indicated by other lines. The line ratios of S XV ( $1s^1 2p^1 \rightarrow 1s^2$ ) at 2.46 keV to S XVI ( $2p^1 \rightarrow 1s^1$ ) at 2.62 keV and Ca XIX ( $1s^1 2p^1 \rightarrow 1s^2$ ) at 3.9 keV to Ca XX ( $2p^1 \rightarrow 1s^1$ ) at 4.11 keV are excellent temperature probes – especially sensitive to the presence of cool gas (see Bulbul et al. (2014b) for discussion). The fluxes of lines from Cl XVII and Ar XVII at 3.51 keV and 3.62 keV are restricted by the other lines of the same ions detected at 2.96 keV and 3.12 keV respectively.

The emissivities of K XVIII, K XIX, Cl XVII, and Ar XVII lines are higher at the lower temperature ranges for each model, which are determined from the S XV to S XVI line ratios. We use factors of 0.1 and 3 over the *highest values within the allowed temperature ranges* for these fluxes as lower and upper bounds for the normalizations of the Gaussian lines as described in Bu14. The factor 3 gives a conservative allowance for variation of the relative elemental abundances between the S and K, Cl, and Ar ions.

### 4.2.1 Systematics

In addition to the atomic model uncertainties (which we account for by using conservatively wide intervals for the allowed fluxes of the atomic lines), the main source of systematic uncertainty regarding the models is the CXB power-law component. In order to estimate the effect of this uncertainty on the other model parameters we perform the following simulations using XSPEC's `fakeit` command. Starting from the best-fit model, a new power-law normalization is randomly drawn uniformly from the  $1\sigma$  range of the originally measured normalization. This is repeated 1000 times, and a simulated spectrum is generated each time (with the input model only differing in power-law normalization). The simulated spectra are refit and from the resulting population the 68% intervals of the distribution for each free parameter are recorded. These are then added in quadrature to the statistical uncertainty from the best-fit model to the real data. The total (statistical and systematic) errors on the best-fit parameters are given in Table 4.4.

Region emitted from	Region detected in			
	0-2	2-4.5	4.5-8.3	>8.3
0-2	0.60	0.33	0.03	0.00
2-4.5	0.09	0.68	0.19	0.01
4.5-8.3	0.00	0.08	0.80	0.08
>8.3	0.00	0.01	0.15	0.78

**Table 4.3:** Percentage redistribution between the inner annuli due to the effects of PSF smearing, as described in Section 4.2.1. Numbers represent the fraction of photons that are emitted from one annulus, and detected in another.

Due to *Suzaku*'s relatively large PSF, some X-ray photons that originate from one particular region on the sky may be scattered elsewhere on the detector. Since the region

sizes we used in this work are similar or relatively large compared to the PSF size of the XIS mirrors, the effect is expected to be small. The effect of PSF spreading on the flux of the  $\sim 3.5$  keV line depends on its origin, and we therefore examine two scenarios. Firstly we consider the case where the flux of the line is distributed according to the broadband X-ray surface brightness as described by the higher resolution imaging of the *XMM Newton* PN observation of the Perseus cluster core (observation ID 0305780101). We use ray-tracing simulations of  $2 \times 10^6$  photons performed through *xissim* (Serlemitsos et al., 2007) with our best-fit model and the PN surface brightness map as input, to determine the scattered photons per sub-region. Table 4.3 reports the results in terms of the fraction of photons that are emitted in one region and detected in the other. These results are consistent with the photon fractions reported in (Bautz et al., 2009) and (Bulbul et al., 2016b). The second scenario that we examine using the same methodology, is when the  $\sim 3.5$  keV line originates from dark matter decay and therefore follows a NFW profile. In this case, the redistribution fraction change only slightly from the ones in Table 4.3, at most by a few percent-points. The dependence on the details of the NFW assumed is even smaller. The net effect of the PSF spreading on the measured fluxes in each regions depends more strongly on the input (or true) distribution than do the redistribution fractions. It is as follows. For the regions 1a through 1c respectively, in the case that the line follows the broadband surface brightness, the measured flux in the line would be underestimated by  $\sim 31\%$ , overestimated by  $\sim 8\%$  and overestimated by  $\sim 22\%$ . In the case that the line flux follows the NFW distribution, the measurement would be underestimated by  $\sim 8\%$ , overestimated by  $\sim 3\%$  and overestimated by  $\sim 2\%$ . In Section 4.5 we will discuss the implications of this on our results, but since the origin of the line at this point is unclear, we will refrain from applying a correction for either scenario in what follows unless explicitly noted.

Model	Reg 1	Reg 2	Reg 3	Reg 4	Reg 2-4
Parameter	(0'–8.3')	(8.3'–25')	(25'–40')	(40'–130')	(8.3'–130')
kT <sub>1</sub> (keV)	3.09 ± 0.04	6.52 ± 0.11	6.10 ± 0.29	5.91 ± 0.50	4.64 ± 0.07
N <sub>1</sub> (10 <sup>-2</sup> cm <sup>-5</sup> )	5.54 <sup>+3.23</sup> <sub>-1.33</sub>	3.69 ± 0.033	0.57 ± 0.016	0.09 ± 0.005	0.60 ± 0.007
kT <sub>2</sub> (keV)	5.78 ± 0.03	-	-	-	-
N <sub>2</sub> (cm <sup>-5</sup> )	0.54 ± 0.04	-	-	-	-
Power-Law Norm (10 <sup>-4</sup> )	7.71 ± 0.65	4.62 ± 1.28	0.00 ± 0.40	0.88 ± 0.10	5.13 ± 0.17
Flux of the S XV	2.71 ± 0.05 × 10 <sup>2</sup>	5.60 ± 4.12	2.06 ± 1.85	0.72 ± 0.64	1.34 ± 0.85
Flux of the S XVI	7.64 ± 0.07 × 10 <sup>2</sup>	23.17 ± 3.45	3.14 ± 1.62	1.21 ± 0.45	5.10 ± 0.70
Flux of the Cl XVII	0.22 ± 0.04 × 10 <sup>2</sup>	-	-	-	-
Flux of the Ar XVIII	2.07 ± 0.04 × 10 <sup>2</sup>	7.35 ± 2.16	-	0.61 ± 0.27	2.11 ± 0.59
Flux of the Ca XIX	1.77 <sup>+0.34</sup> <sub>-0.17</sub> × 10 <sup>2</sup>	3.96 ± 4.56	1.14 ± 0.98	-	1.07 ± 0.55
Flux of the Ca XX	1.43 ± 0.03 × 10 <sup>2</sup>	4.7 ± 1.69	-	-	0.93 ± 0.39
χ <sup>2</sup> (dof)	2504.4 (2170)	2919.0 (3061)	3276.1 (3063)	3880.3 (3062)	3259.0 (3060)

**Table 4.4:** The best-fit parameters of the model. The fluxes of the S XV, S XVI, Cl XVII, Ar XVIII, Ca XIX, and Ca XX lines are in the units of 10<sup>-6</sup> ph cm<sup>-2</sup> s<sup>-1</sup>. Fields with a '-' indicate the absence of this component from the model. The χ<sup>2</sup> reported does not include a  $\sim 3.5$  keV model component.

Model	Reg 1a	Reg 1b	Reg 1c
Parameter	(0'-2')	(2'-4.5')	(4.5'-8.3')
kT <sub>1</sub> (keV)	3.35 ± 0.11	4.85 ± 0.04	6.41 ± 0.22
N <sub>1</sub> (10 <sup>-2</sup> cm <sup>-5</sup> )	0.11 ± 0.03	0.12 ± 0.06	0.22 ± 0.01
kT <sub>2</sub> (keV)	5.72 ± 0.29	6.02 ± 0.24	-
N <sub>2</sub> (cm <sup>-5</sup> )	0.16 ± 0.04	0.20 ± 0.03	-
Power-Law Norm (10 <sup>-4</sup> )	4.16 ± 0.51	1.77 ± 0.63	5.11 ± 0.16
Flux of the S XV	1.74 ± 0.07	1.44 ± 0.16	0.65 ± 0.16
Flux of the S XVI	4.39 ± 0.07	4.20 ± 0.07	1.99 ± 0.09
Flux of the Cl XVII	0.28 ± 0.06	-	-
Flux of the Ar XVIII	1.31 ± 0.13	1.19 ± 0.07	0.39 ± 0.11
Flux of the Ca XIX	1.14 ± 0.12	1.03 ± 0.04	0.39 ± 0.05
Flux of the Ca XX	0.71 ± 0.04	0.78 ± 0.05	0.48 ± 0.04
χ <sup>2</sup> (dof)	2317.3 (2168)	2450.8 (2168)	2401.7 (2168)

**Table 4.5:** Same as Table 4.4, but for the subregions of the core. The best-fit parameters of the model. The fluxes of the S XV, S XVI, Cl XVII, Ar XVIII Ca XIX, and Ca XX lines are in the units of 10<sup>-4</sup> pht cm<sup>-2</sup> s<sup>-1</sup>. Fields with a '-' indicate the absence of this component from the model.

## 4.3 Results

### 4.3.1 Perseus Center

We initially extract source and background spectra from a circular region surrounding the cluster's center with a radius of 8.3' (we refer to this region as *Region 1*). The total filtered on-axis FI/BI exposure times are 1.0/0.67 Ms. There are  $1.4 \times 10^7$  source counts in the background-subtracted FI spectrum and  $1 \times 10^7$  in the BI spectrum

We model the 1.95 to 6 keV band with the continuum and lines as described in the previous section (Section 4.2). The best-fit values of the model are given in Table 4.4. The plasma temperature measured from the continuum ( $3.09 \pm 0.04$  keV) is in agreement with the plasma temperature estimated from the S XV to S XVI line flux ratio (3.13 keV) at a  $1\sigma$  level. We stress again that the S line ratio is very sensitive to cool gas. The peak emissivity of the S XV line is at  $kT \approx 1$  keV; thus, if any significant cool gas phase were present, the line ratio temperature would be biased toward it. This plasma temperature is also in good agreement with the temperatures measured from the *XMM-Newton* and *Chandra* observations of the Perseus cluster (Bulbul et al., 2014a,b).

Estimating the fluxes of detected lines is crucial for determining the flux around the 3.5 keV line. For a sanity check, we compare the intensities of the three lines from ions (i.e., Si XIV, Ar XVII, Cl XVII) detected significantly in the fitting band with the estimates based on the observed S XV / S XVI line ratio. Si XIV line at 2 keV is detected significantly with a flux of  $(1.24 \pm 0.01) \times 10^{-3}$  pht cm<sup>-2</sup> s<sup>-1</sup>. The predicted Si XIV flux from a

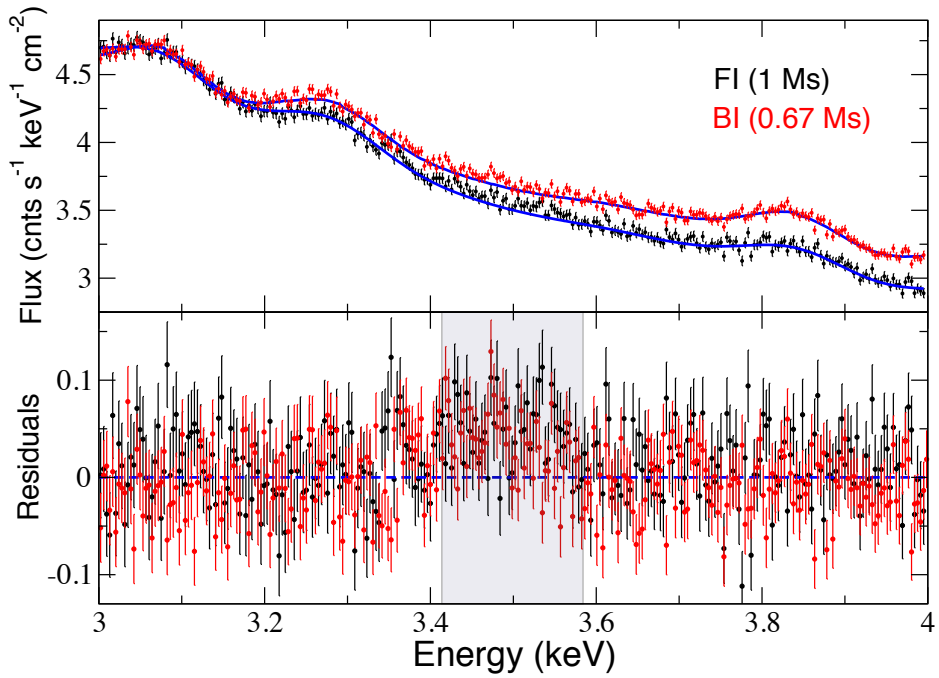


**Figure 4.2:** Observed *Suzaku* FI and BI Spectrum of the Perseus cluster core (Region 1). The residuals around 3.5 keV (redshifted) are visible clearly (shaded area in the bottom panel). The model shown in the figure includes contributions from the nearby K XVIII, Cl XVII, and Ar XVII lines. The 3.5 keV rest-frame energy corresponds to 3.49 keV in this plot.

$\sim 3.1$  keV plasma is  $1.38 \times 10^{-3}$  pht  $\text{cm}^{-2} \text{s}^{-1}$  using AtomDB, indicating that S and Si have relative abundances of  $0.9 \pm 0.01$  with respect to the Asplund et al. (2009) solar abundances. The measured Ar XVII at 3.12 keV is  $2.07 \pm 0.41 \times 10^{-4}$  pht  $\text{cm}^{-2} \text{s}^{-1}$ , while the flux estimated using AtomDB is  $1.30 \times 10^{-4}$  pht  $\text{cm}^{-2} \text{s}^{-1}$ . The implied abundance ratio of Ar to S is  $1.6^{+0.31}_{-0.32}$  with respect to the solar abundance. Unlike in the stacked *XMM-Newton* observations of a large sample of clusters and the *XMM-Newton* and *Chandra* observations of the Perseus cluster (from Bo14 and Bu14), we detect a very faint Cl Ly- $\alpha$  line at 2.96 keV in the *Suzaku* spectrum of the Perseus core. The measured  $(2.20 \pm 0.4) \times 10^{-5}$  pht  $\text{cm}^{-2} \text{s}^{-1}$  and estimated ( $1.93 \times 10^{-5}$  pht  $\text{cm}^{-2} \text{s}^{-1}$ ) Cl Ly- $\alpha$  fluxes indicate that the abundance ratio of Cl to S is  $\sim 1.1^{+0.25}_{-0.18}$  with respect to the solar abundance. The best-fit flux of the K XIX line at 3.70 keV is  $6.0 \pm 4.0 \times 10^{-6}$  pht  $\text{cm}^{-2} \text{s}^{-1}$ . The predicted flux of the line ( $3.4 \times 10^{-6}$  pht  $\text{cm}^{-2} \text{s}^{-1}$ ) shows that the abundance ratio of K to S is  $1.8 \pm 1.2$  with respect to solar.

Parameter	Reg 1	Reg 1a	Reg 1b	Reg 1c	Reg 2	Reg 3	Reg 4	Reg 2-4
kT based on S (keV)	3.13 $\pm$ 0.03	2.97 $\pm$ 0.06	3.18 $\pm$ 0.17	3.25 $\pm$ 0.36	3.74 $^{+1.23}_{-1.69}$	2.37 $^{+0.90}_{-2.37}$	2.47 $^{+0.90}_{-1.56}$	3.60 $^{+1.00}_{-1.34}$
kT based on Ca (keV)	4.02 $\pm$ 0.29	3.65 $\pm$ 0.16	3.92 $\pm$ 0.11	4.85 $\pm$ 0.36	4.77 $^{+2.32}_{-4.77}$	–	–	4.14 $^{+1.11}_{-1.36}$
Flux of Cl XVII at 2.96 keV	1932.9	1085.6	1068.9	510.8	62.2	6.79	2.70	13.5
Flux of Cl XVII at 3.51 keV	295.3	164.8	163.6	78.4	9.69	1.00	0.40	2.10
Flux of K XVIII at 3.47 keV	227.8	138.3	122.6	56.4	5.32	1.13	0.43	1.25
Flux of K XVIII at 3.49 keV	112.4	68.2	60.5	27.9	2.65	0.57	0.22	0.62
Flux of K XVIII at 3.51 keV	471.1	280.1	255.3	118.5	11.8	2.13	0.82	2.73
Flux of Ar DR XVII at 3.62 keV	56.9	38.1	29.8	13.1	0.97	0.50	0.17	0.24

**Table 4.6:** Estimated fluxes of the Cl XVII, K XVIII, Ar DR XVII lines are in the units of  $10^{-8}$  pht  $\text{cm}^{-2} \text{s}^{-1}$  from AtomDB. The fluxes (and not the temperature) in this table are dependent on the assumed solar abundance (Asplund et al., 2009), and are employed in the fits by setting the upper and lower allowed limits for the fitting procedure to 3 times and 0.1 times this flux, respectively. Temperature ranges implied by uncertainty of the measured lines are shown for illustrative purposes.

To estimate the flux of the 3.5 keV line, we model the possibly contaminating K XVIII (3.47 keV: 3.49 keV: 3.51 keV), and Ar XVII (3.12 keV: 3.62 keV: 3.68 keV) lines with the ratios of (1: 0.5: 2.3) and (1: 1/23: 1/9). The line ratios are estimated for the temperature indicated by the observed S XVI/XV line ratio. We also include the Cl Ly- $\beta$  line at 3.51 keV with a flux tied to  $0.15 \times$  that of the the flux of the Cl Ly- $\alpha$  line at 2.96 keV in our fits. The measured best-fit K XVIII at 3.51 keV is  $1.05 \times 10^{-6}$  pht  $\text{cm}^{-2} \text{s}^{-1}$ , also in agreement with the AtomDB predictions. We note that the total flux of the K XVIII triplet between 3.47–3.51 keV is estimated at  $8.11 \times 10^{-6}$  pht  $\text{cm}^{-2} \text{s}^{-1}$  from AtomDB (Table 4.6), but that we allowed the K XVIII flux to be up to  $2.5 \times 10^{-5}$  pht  $\text{cm}^{-2} \text{s}^{-1}$  in our fits. Additionally, we provide the flux estimates of the detected lines based on Anders & Grevesse (1989) solar abundance for comparison in Appendix 4.6 as Table 4.9. In summary, the abundance ratios of detected lines implied by our measurements and AtomDB range between 1–1.7 for the strongly detected lines (including K XIX) in our fitting band, well within the assumed interval of a factor 0.1–3 regardless of assumed solar abundance sets.

Examining the 3–4 keV band in the simultaneous fits of the FI and BI observations, we find excess emission around 3.5 keV (rest energy). The residuals around 3.5 keV

(which corresponds to a redshifted energy of 3.49 keV) are shown in Figure 4.2. If we add a redshifted Gaussian line with energy as a free parameter, the best-fit energy of the line becomes  $3.54 \pm 0.01(0.02)$  keV with a flux of  $2.79_{-0.35}^{+0.35} \left( {}_{-0.57}^{+0.59} \right) \times 10^{-5}$  pht cm $^{-2}$  s $^{-1}$ . The fit improves by  $\Delta\chi^2$  of 62.6 for 2 degrees-of-freedom (d.o.f.), corresponding to a  $\sim 7.6\sigma$  detection.

To investigate the radial behavior of the signal in the core, we divided the core into three spectral extraction regions: circular regions with radii of 0–2', 2'–4.5', and 4.5'–8.3'. The best-fit model parameters of the *line-free apec* model is given in Table 4.6. Following the same fitting procedure described above, we find that the best-fit energy and flux of the line in the innermost 0–2' region are  $3.51 \pm 0.02$  (0.03) keV and  $9.28_{-2.67}^{+2.62} \left( {}_{-4.33}^{+4.41} \right) \times 10^{-6}$  pht cm $^{-2}$  s $^{-1}$ . The change in the  $\Delta\chi^2$  is 12.1 for the extra 2 d.o.f. In the intermediate 2'–4.5' region, the line energy is detected at  $3.55 \pm 0.02$  (0.03) keV with a flux of  $1.67_{-0.30}^{+0.29} \left( {}_{-0.48}^{+0.52} \right) \times 10^{-5}$  pht cm $^{-2}$  s $^{-1}$  ( $\Delta\chi^2=23.3$  with additional two d.o.f.). The line is also detected in the last 4.5'–8.3' region at an energy of  $3.58 \pm 0.02$  (0.03) keV with a flux of  $1.61_{-0.34}^{+0.32} \left( {}_{-0.49}^{+0.51} \right) \times 10^{-5}$  pht cm $^{-2}$  s $^{-1}$  ( $\Delta\chi^2=16.5$  for additional 2 d.o.f.). The radial profile of this signal has also been studied by Urban et al. (2015) in two spectral regions. Our results are in broad agreement once the sizes and shapes of the spectral extraction regions are taken into account, as we will discuss in Sections 4.4.

We then fit these spectra with a Gaussian model with the line energy fixed at 3.54 keV, which is the best-fit value detected in the 0–8.3' region. We find that the flux of the line becomes  $6.54 \pm 2.62$  (4.3)  $\times 10^{-6}$  pht cm $^{-2}$  s $^{-1}$  in the innermost 0–2' region, with a change in the  $\Delta\chi^2=6.23$  for an additional 1 d.o.f. The flux remains the same ( $1.67_{-0.28}^{+0.31} \left( {}_{-0.47}^{+0.49} \right) \times 10^{-5}$  pht cm $^{-2}$  s $^{-1}$ ) within the intermediate 2'–4.5', while the change in the  $\chi^2$  becomes 25.9 for an additional 1 d.o.f. In the last region the line is detected with a flux of  $1.27_{-0.34}^{+0.29} \left( {}_{-0.47}^{+0.41} \right) \times 10^{-5}$  pht cm $^{-2}$  s $^{-1}$  with a  $\Delta\chi^2$  of 10.8 for additional 1 d.o.f. The  $\sim 3.5$  keV line is detected with a confidence of  $> 3\sigma$  in all three regions within the core of the Perseus cluster. Table 4.7 summarizes the above results.

### 4.3.2 Perseus Outskirts

A total of 100 *Suzaku* observations of the Perseus cluster with the nominal pointing further than 14' from the cluster center were retrieved from the archives, for a total cleaned FI/BI exposure of 2.72/1.36 Ms and background-subtracted source counts of  $6.3 \times 10^5$  and  $4.3 \times 10^5$ . We divide this data into three annular spectral extraction regions. The first annulus (called 'Region 2') starts at 8.3', where the central analysis of Section 4.3.1 ends, and extends to 25'. 'Region 3' is an annular extraction region with inner radius 25', and outer radius 40'. While the outermost annulus does not have an outer radius imposed, the outermost pointing is centered on 117' from the Perseus cluster core, so that all data used in this study comes from within 130'. This is 'Region 4' in Table 4.1. The same table contains the sizes of all regions in angular and physical scales. A visual representation is given in Figure 4.1. As will become apparent in later sections, it is also useful to create a single stacked dataset of all these off-center observations in order to obtain better statistics. This is referred to as 'Region 2-4' in Table 4.1.

To further obtain maximum photon statistics, in the results reported here for the off-center data, no point sources were removed. A parallel analysis of a version of the dataset

Region		Restframe E	Flux	$\Delta\chi^2$	$\chi^2$ (dof)
		keV	$10^{-5} \text{ ph s}^{-1} \text{ cm}^{-2}$		
Region 1	(0'–8.3')	$3.54 \pm 0.01(0.02)$	$2.79^{+0.35}_{-0.35} (+0.59/-0.57)$	62.6	2441.7 (2168)
Region 1a	(0'–2')	$3.51 \pm 0.02(0.03)$	$0.93^{+0.26}_{-0.27} (+0.44/-0.43)$	12.1	2317.3 (2168)
		3.54	$0.65 \pm 0.26(0.43)$	6.23	
Region 1b	(2'–4.5')	$3.5 \pm 0.02(0.03)$	$1.67^{+0.29}_{-0.30} (+0.52/-0.48)$	23.3	2450.8 (2168)
		3.54	$1.67^{+0.31}_{-0.28} (+0.49/-0.47)$	25.9	
Region 1c	(4.5'–8.3')	$3.58 \pm 0.02(0.03)$	$1.61^{+0.32}_{-0.34} (+0.51/-0.49)$	16.5	2401.7 (2168)
		3.54	$1.27^{+0.29}_{-0.34} (+0.41/-0.47)$	10.8	

**Table 4.7:** Best-fit values for detected excess emission around 3.5 keV (rest frame) for the core regions. Also included is the best-fit flux in the case that the energy is fixed to the best fit from Region 1 (ie, 1 additional degree-of-freedom instead of 2). Total  $\chi^2$  values are shown before the  $\sim 3.5$  keV line is added to the model.

with the point sources removed as detected by Urban et al. (2015), did not reveal large qualitative differences. Since we have not detected the 3.5 keV line in the outskirts, we only show the higher-statistics dataset that did not mask the point sources.

The spectral modeling of the off-center is performed as described in Section 4.2, unless noted otherwise. The energy band used for fitting the off-center observations is reduced to 1.95 – 5.7 to avoid a strong negative residual in the XIS 1 spectra. This is likely associated with an imperfect background subtraction of the instrumental Mn-K $\alpha$  line (see also Sekiya et al. (2015)). In addition to the tied line ratios mentioned in Section 4.2, the off-center analysis also tied the flux of the S XV line at 3.03 to S XV at 2.46 with the theoretical ratio (1:40).

As in the analysis of the central region, we utilize the observed line ratios of S and Ca where available to determine the maximum contribution of the Ar and K lines near 3.5 keV. The measured line ratios in most regions imply a second thermal component at somewhat lower temperature, but none of the broadband fits prefer a model with two plasma continuum components. As we noted in the previous section, this is not entirely unexpected for a multi-temperature environment as the broad-band fit is mostly sensitive to high temperatures and the power-law normalization of the CXB component, while the emissivity of the S lines peaks at low temperatures and thereby causes the S line ratios to be sensitive to the low temperature components. Therefore we modify the previously obtained models by setting the maximum allowed range for the line normalizations for the Ar, K and Cl lines around 3.5 keV to  $3 \times$  the maximum shown in Table 4.6 indicated by the S and Ca ratios, and refitting.

We obtained acceptable fits to the data of all off-center regions with a reduced- $\chi^2$  of around 1, except for Region 4 (the outer region), where  $\bar{\chi}^2 \sim 1.25$ . This is most likely due to large radial extent of this region of the cluster that is stacked, making the single model fit insufficient. The results of the fits of the off-center regions are shown in table 4.4.

Plasma temperatures and normalizations are generally consistent with the measurements performed by Urban et al. (2014). However, the relatively low best-fit temperature for Region 2-4 is mainly caused by a preference for a relatively high normalization of the powerlaw. Fixing the powerlaw normalization to a lower value more in line with the outer regions, brings the temperature of the continuum component up again to above 6 keV. However, the fit with the fixed powerlaw normalization provides a worse fit by a  $\Delta\chi^2$  of about 15. The fit otherwise shows no qualitative differences, and therefore we continue to employ the better fitting model (with fitted powerlaw normalization). As mentioned above, the best-fit continuum temperature is not used for the estimates of line strengths, rather the line ratios of well-measured S- and Ca- lines are.

With these final models in hand, we look for the presence of excess emission by adding a redshifted Gaussian line component to the model at different restframe energies around  $\sim 3.5$  keV while leaving the normalization free. The plasma temperature and the normalizations of all other model components are left free in these fits. There is not a single region of the Perseus cluster outskirts for which we see significant positive line-like residuals anywhere in the vicinity of 3.5 keV (restframe). Note that none of the Ar, Cl or K lines near 3.5 keV are detected in these datasets either (i.e., contributions from these lines were allowed in the earlier fitting process described in Section 4.2, but were not required by the fits).

Not having found significant line-like residuals around 3.5 keV, we compute the flux limit for such a line for each off-center spectrum in the following way. Starting with the best-fit model we add one redshifted Gaussian at rest-frame 3.54 keV (the nominal detected value in Region 1), and vary its normalization until the new  $\Delta\chi^2$  is higher by 4.0, which corresponds to a  $2\sigma$  limit for a single added degree of freedom. The normalizations of all model components are left free, as is the plasma temperature. The obtained flux limits will be discussed in Section 4.4.1.

## 4.4 Discussion

### 4.4.1 Line Flux and Dark Matter Profiles

We compare our results to the behaviour expected from dark matter decay in this Section. For a first look, Figure 4.3 shows the radial dependence of the surface brightness of the  $\sim 3.5$  keV signal. The results from this work and those obtained by Bo14 are shown in red and blue respectively. Downward pointing arrows indicate the  $2\sigma$  upper limits from the analysis of the outskirts. Expected dark matter decay signal strength for different NFW dark matter distributions (see below) is depicted by the set of black curves. It is important to note that the normalization of the expected decay signal depends on the dark matter particle lifetime and is therefore completely degenerate with the absolute mass scale of the NFW profiles. The figure shows arbitrary individual normalizations chosen to facilitate visual comparison in this case.

Additionally, Figure 4.3 shows the detected surface brightness of the Fe XXV K- $\alpha$  line at 6.7 keV from all our *Suzaku* regions with the open purple squares as an indicative visual example of possible emission line-like behaviour. This behaviour is typically described by a double- $\beta$  profile, which is shown as the purple dashed line with parameters from Churazov et al. (2003) albeit with arbitrary overall normalization in order to roughly line

up with the Fe measurements. The measurements of the Fe lines and the double- $\beta$  profile are compatible with each other while showing quite a contrast with both the  $\sim 3.5$  keV measurements and the DM decay-like profiles.

It is important to note that the radial behaviour as shown in this figure does not accurately reflect the effects of the varying pointings nor of the varying field-of-view shapes and sizes that are averaged in each datapoint, which will be handled in detail in the following.

Are our non-detections in the Perseus outskirts inconsistent with the dark matter decay origin of the 3.5 keV line? In order to determine this, we compare the measurements to the predictions in the most direct way, by computing the effective dark matter mass in the field of view for each dataset. For a given field of view, this quantity depends only on the dark matter profile assumed, and is directly related to the expected signal by the particle lifetime. It is computed as follows. For the off-center *Suzaku* data, where the different observations have been separated into concentric annuli, we divide the available pixels for a particular observation and extraction region into 25 spatial bins. Then we compute the dark matter column density at the center of each of those bins, given an NFW model, before converting to mass inside the effective field-of-view using the effective sky area. The exposure weighted average mass is then obtained for each region. For the on-axis observations, the extraction regions are of a more convenient shape, allowing us to simply compute the enclosed mass within a certain projected radius for a given NFW profile.

We compare the results of this work with the results obtained in Bo14, Bu14 and Urban et al. (2015). The effective dark matter mass for these observations is obtained in a similar fashion as described above. Figure 4.4 shows the flux (detections and upper limits) of the  $\sim 3.5$  keV line as a function of dark matter mass in the field of view for a bracket of literature mass profiles. The red boxes marked *Suzaku* are the detections and the upper limits from this work (upper limits defined as  $\Delta\chi^2$  of 4.0, or  $2\sigma$  for 1 degrees of freedom). Lines of constant dark matter particle lifetime are shown as diagonal black lines. Each box represents a different spectral extraction region, for which the DM mass in that particular field of view has been computed by the method described above. This is done for three literature profiles for the Perseus cluster (e.g., Simionescu et al., 2012a; Sánchez-Conde et al., 2011; Storm et al., 2013). Storm et al. (2013) makes use of the measurement of  $M_{500}$  of Chen et al. (2007), determines NFW parameters through scaling relations and finally corrects for the gas fraction to get to the dark matter distribution. Sánchez-Conde et al. (2011) employs the measurement of  $M_{200}$  from Reiprich & Böhringer (2002) and the scaling relation from Duffy et al. (2008). Lastly, Simionescu et al. (2012a) derives an NFW profile for the total mass distribution directly by fitting to piecewise annular X-ray data. The latter two do not quote dark matter only profiles, so we take the baryon fraction into account using the functional form  $f_{gas} \sim r^{0.43}$  (Mantz et al., 2014) calibrated to the reported gas fraction of Perseus by Simionescu et al. (2012a). Included in the bracket of computed enclosed dark matter mass are the statistical  $1\sigma$  uncertainties reported in those works, although the scatter between the different profiles is larger than the statistical errors on each. In all computations of the enclosed dark matter mass, the different background cosmologies and differences in the definition of the NFW used in those studies have been taken into account.

Here we take the effects of PSF smearing described in Section 4.2.1 into account in the following way. As was noted, this effect is only relevant for the smaller regions 1a

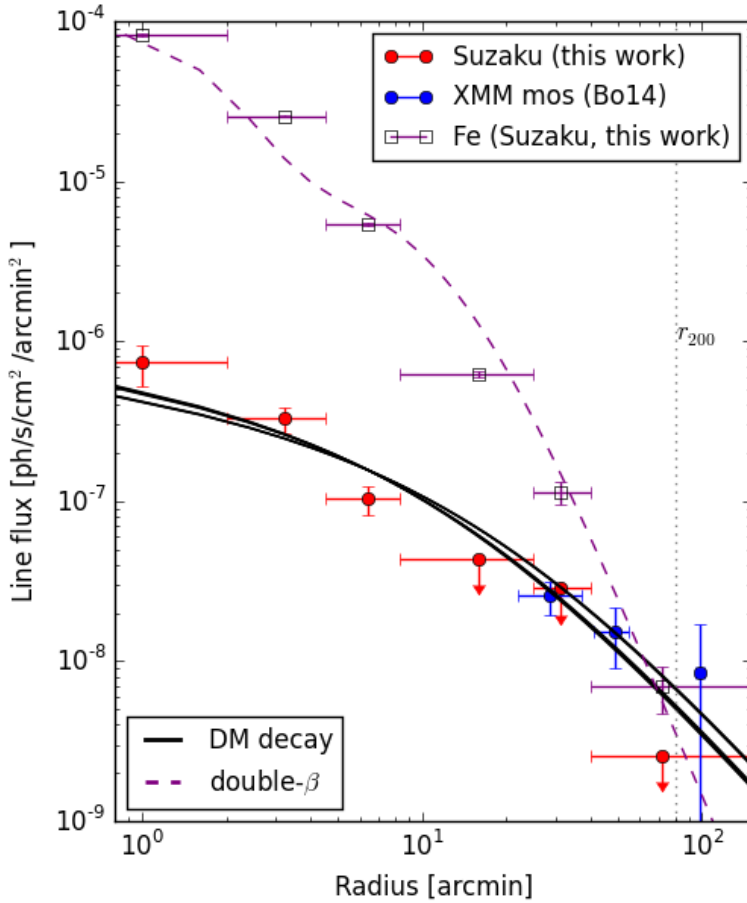


**Figure 4.3:** Radial profile of the measured  $\sim 3.5$  keV surface brightness ( $1\sigma$  error bars) and upper  $2\sigma$  limits obtained from our Suzaku measurements (red), compared to the measurements of Bo14 using *XMM-Newton* (blue). Black curves indicate the expected surface brightness profiles of a dark matter decay signal based on several NFW literature profiles for the dark matter distribution (see text). The normalization of these predictions is degenerate with the particle lifetime, and the shown curves have an arbitrary normalization assigned for visual purposes in this figure. Horizontal error bars show the bracket of radial extraction regions per bin, while the central value is the dark matter column density-weighted average radius for that radial bin. For comparison, the purple empty squares indicate measurements of the Fe  $_{XXV}$  K- $\alpha$  emission at 6.7 keV in our data and the purple dashed curve shows a surface brightness profile based on the double- $\beta$  profile measured by Churazov et al. (2003) but with arbitrary normalization. Note that none of the lines shown in this figure are fitted.

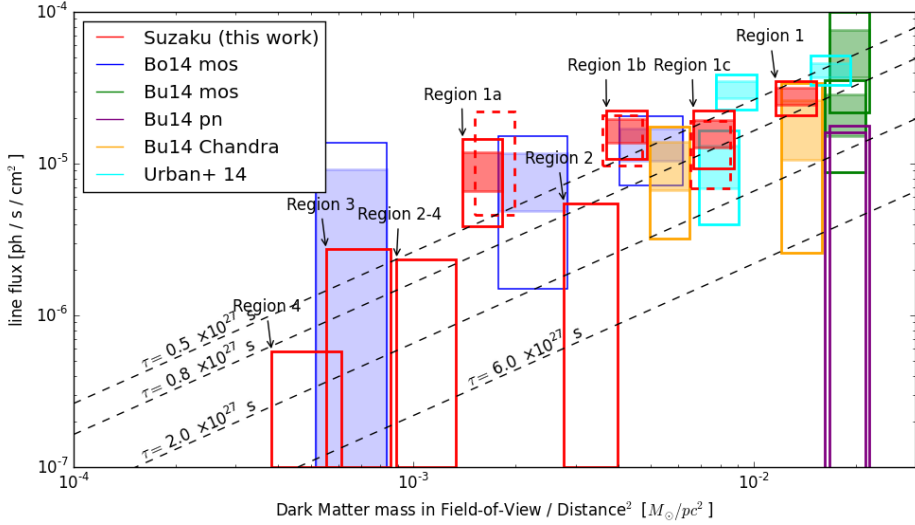


**Figure 4.4:** The 3.5 keV flux as a function of the dark matter mass in the field of view. Measured by *Suzaku* in the red boxes (this work), by *XMM-Newton* MOS from Bo14 in blue and from Bu14 in green, by *XMM-Newton* PN in purple (Bu14), by *Chandra* in orange (Bu14). Also shown in cyan are the *Suzaku* measurements of Urban et al. (2015) with from left to right their 'confining', 'core' and full extraction regions (see text). Filled boxes indicate  $1\sigma$  flux measurements, open boxes the  $2\sigma$  interval. Boxes without a filled part and touching the x-axis indicate upper limits ( $2\sigma$  for this work, reported 90% for Bu14 pn), i.e., Bu14 pn, and Regions '2', '3', '4' and '2-4'. The dashed red boxes indicate  $2\sigma$  intervals of the *Suzaku* core subregions that have been corrected for PSF scattering using an alternative scenario for its estimation (see Sections 4.2.1 and 4.5). The width of the boxes is given by the bracket of different literature NFW profiles (see text). Lines of constant dark matter particle lifetime are the black lines with decay rates given in the annotation. NB: this study does not constrain the value of  $\tau$  as this requires and absolute mass scale to be established; the values shown are for indicative purposes. The study by Boyarsky et al. (2015) compares different objects to this end, and uses a broader mass bracket for the Perseus cluster due to the inclusion of additional different probes of the cluster mass, extending the brackets out to longer lifetimes of order  $\tau \sim 6 \times 10^{27}$  (see Section 4.4.1 for discussion).

through 1c, and it is dependent on the origin of the  $\sim 3.5$  keV line. In Figure 4.4, we compare the measured flux to the expected flux for a dark matter decay scenario, and we therefore apply the estimated effects of this scenario to the boxes for Regions 1a through 1c (we repeat for convenience; -8%, +3%, +2% respectively). For completeness we also show the corrections for the scenario when the  $\sim 3.5$  keV line follows the broadband X-ray surface brightness (as described in Section 4.2.1, -31%, +8%, +22%) as the dashed open red boxes. In both cases, this systematic effect was also added in quadrature to the error estimate to account for the uncertainty on this effect itself. Qualitatively, our conclusion is independent of the approach to PSF smearing used.

Not all data in Figure 4.4 is statistically independent. Regarding the current work (red boxes), ‘Region 2-4’ is a compound of ‘Region 2’, ‘Region 3’ and ‘Region 4’. Regions 1a-c are subdivisions of ‘Region 1’. Bu14 reported 2 measurements for each of the mos (green boxes) and pn detectors (purple boxes), the difference being the excision of the central 1’ of the Perseus cluster (the data with the core excluded is the datapoint with the lower effective dark matter mass). Their *Chandra* measurements (yellow boxes) refer to the ACIS-S and ACIS-I chips of which the latter has the larger field-of-view and therefore higher effective dark matter mass. The 3 measurements shown of Urban et al. (2015) (cyan boxes), from right to left (higher to lower effective dark matter mass), refers to their full extraction region (full *Suzaku* field-of-view on-center), the core of the Perseus cluster (inner 6’) and the ‘confining’ region (full field-of-view excluding the 6’ core). In addition, the Urban et al. (2015) study is based on the same archival data as our ‘Region 1’ (and its sub-divided annuli). The Bo14 and Bu14 mos data from *XMM-Newton* are in fact from different independent pointings.

Our results as shown in Figure 4.4 indicate that the measurements and upper limits obtained with *Suzaku* in this work are internally mostly consistent with a decaying dark matter interpretation and with previous measurements. However, the non-detection in the outer-most region (‘Region 4’) is somewhat at odds with the fluxes of the measurements of the inner 2’ (‘Region 1a’) and the annulus between 2’ and 4.5’ (‘Region 1b’). Here we note that ‘Region 4’ has the worst fit quality of all off-center datasets at a reduced- $\chi^2$  of  $\sim 1.25$  and the upper limit may be affected by this. In addition, the limit from Region 2 is marginally inconsistent with the detection in ‘Region 1b’.

The very core of the Perseus cluster exhibiting relatively high  $\sim 3.5$  keV flux as reported in previous works is confirmed in our *Suzaku* data, but the inconsistency is less than  $3\sigma$  even in the most extreme case. In addition, this enhanced flux is confined to a region smaller than  $\sim 100$  kpc (or  $\sim 4.5'$ ), a large fraction of which is occupied by the brightest cluster galaxy NGC 1275, and which is well inside the cool-core. This may influence both the spectral modeling and the dark matter distribution. Lastly, relaxing our conservative bounds (defined as  $\Delta\chi^2$  of 4.0 for a fixed line energy) on the non-detections will alleviate the above inconsistencies.

The NFW profiles implemented in our calculations are taken from the literature as reported, all of which are based on X-ray measurements. Boyarsky et al. (2015) uses additional literature profiles obtained by different methods for the comparison between different objects, whereas this work is concerned with the internal behaviour of the signal within the Perseus cluster only. Extending the mass bracket to include all of the profiles used in Boyarsky et al. (2015) (not shown),  $\tau = 6 \times 10^{27}$  s becomes consistent with almost all measurements. We stress again that absolute mass calibration is degenerate with dark

matter particle lifetime  $\tau$  and that this work therefore does not constrain the latter.

#### 4.4.2 Discussion of Perseus' Morphological and Dynamical State

The use of an NFW profile for the dark matter distribution of the Perseus cluster is justified, as the cluster is reported to be a relatively relaxed cluster with a regular morphology and a moderately strong cool core (Simionescu et al., 2012a,b). These studies find that even if the assumptions of spherical symmetry and hydrostatic equilibrium are relaxed to account for some evidence of gas clumping (Simionescu et al., 2012a), their results remain consistent. In addition, the in- or exclusion of data from additional instruments, nor a change to a generalized NFW profile influence those results. Simionescu et al. (2012b) do report evidence of a past minor merger, indicated by a spiral-pattern of enhanced surface brightness across the extent of the Perseus cluster in *Suzaku* data due to gas sloshing. The infall trajectory has been determined as east-west, although the inclination is ill-constrained other than excluding edge-on. The initial NFW profile determined by Simionescu et al. (2012a) was based on observations of the North-West-arm of the *Suzaku* survey of the Perseus cluster. This arm does not exhibit any evidence of this minor merger, so it is safe to conclude that for the current work it is not required to allow for any additional uncertainty in the mass profile of the Perseus cluster to account for dynamical disturbance, or irregular morphology.

#### 4.4.3 Literature Comparison

The data of the Perseus core from the *Suzaku* archives employed in this work was also used by Urban et al. (2015) and Tamura et al. (2015). These works contain contradictory results, with Tamura et al. (2015) not reporting any excess flux around  $\sim 3.5$  keV. Our results agree with the work of Urban et al. (2015) regarding the Perseus cluster. Although our extraction regions and the spectral modeling are different, the  $\sim 3.5$  keV line surface brightness is consistent once the different spectral extraction regions are taken into account (as can be seen in Figure 4.4).

The work by Tamura et al. (2015) is unable to detect the putative feature at  $\sim 3.5$  keV in the same data as employed in the present work and by Urban et al. (2015) even though we employ the same calibration modifications (see Section 4.2) as Tamura et al. (2015). The authors claim that the  $\sim 3.5$  keV line detection could be an artifact of the degeneracy between the atomic lines and the continuum during fitting. They illustrate their claim with an example (in their section 4.2 and figure 14), where they fit the data between 3 – 4.2 keV with a model consisting of the plasma continuum and nine additional emission lines. Removing one of the lines from this model reveals a positive line-like residual, by design. There are a number of issues with this particular approach. Firstly, their fitting band is too narrow to determine the continuum level accurately, and in addition, they cover their entire energy range with extra gaussian lines, practically guaranteeing complete degeneracy between line fluxes and continuum level given the large resolution of XIS detectors. Secondly, the lines that are added are given fluxes that are unphysically high, namely 0.2 times the 3.1 keV Ar line, whereas our Table 6 shows that that these lines are expected to be about 10 times lower (0.03 – 0.04 times the 3.1 keV Ar flux) than that. These fluxes were not allowed to vary and forced to be overestimated in their

fit. This forces their continuum level to be underestimated, again guaranteeing that the removal of one gaussian model component reveals a line-like residual. A possible way to test this would be to compare the plasma temperature estimates, however, the plasma temperatures are not provided in the relevant section.

Additionally, the line modeling in Tamura et al. (2015) is less exhaustive than in our work (their 9 atomic lines compared to our 29). The limited number of lines used in their analysis leads to a large reduced chi-square value of 1.72 (compared to our 1.1). Indeed, most of the line emission does not get modeled properly and leads to residuals that are larger than the putative feature we detected in the fitting band. We reiterate that the putative feature is only a 1% flux feature over the continuum and that the continuum should be modeled at that level or better to be able to detect the line. We agree that the quality of the spectral modeling is essential to our work, and that at CCD resolution one has to be very careful of the interplay between atomic lines and the continuum. Our modeling procedure is as thorough as it is, taking the widest possible energy range to help determine the continuum level, providing physically motivated modeling of the atomic lines, and cross-checking the best fit line fluxes with atomic data.

## 4.5 Conclusion

We have studied all available data from the *Suzaku* telescope of the Perseus cluster out to almost  $1.5r_{200}$  with the aim to investigate the radial behavior of the still unidentified line feature around 3.5 keV that was first reported in Bu14 and Bo14. We have studied the possibility that the detected 3.5 keV feature in the center of the Perseus cluster is due to atomic emission from highly-ionized nearby Ar XVII, Cl Ly- $\beta$ , and K XVIII lines in the spectral neighborhood. We detect, for the first time, Cl Ly- $\alpha$  line at 2.96 keV in clusters of galaxies, whose flux is used to calculate the flux contribution of Cl Ly- $\beta$  line at 3.5 keV. Using measurements of various detected strong emission lines in other energy bands of the spectrum to estimate the plasma temperature and allowing for a conservatively large range of elemental abundances, we find that the 3.5 keV flux is in excess of what is allowed for atomic line emission. We report a detection of this line feature from the central observations of the Perseus cluster with a measured flux in agreement with the previously reported detection (Urban et al., 2015).

The *Suzaku* observations of the cluster's outskirts do not exhibit an excess of flux around 3.5 keV, nor in radially separated annular regions. The upper limits provided by the co-added outskirts observations are consistent with the dark matter decay interpretation for the origin of the signal from the Perseus cluster. Of course, our results are also consistent with some unknown astrophysical line originating predominantly in the dense gas of the Perseus core.

Considering the current body of work, it is not presently possible to prove conclusively the origin of the 3.5 keV line as sourced by any one process. The measurements in this study indicate that cluster outskirts or other low-density environments are promising targets in terms of constraining power for future observational work provided the exposure reaches deep enough. The most likely immediate-future gain is through employing next-generation micro-calorimeters on board the planned *Micro-X* (Figueroa-Feliciano et al., 2015) mission, or on board *Hitomi* (Kitayama et al., 2014) if the satellite or any data

thereof can be salvaged. These instruments have the energy resolution required to improve the spectral modeling, in particular with regards to the measurements of the various line emission. Alternative methodologies relying on different observables to distinguish dark matter decay from astrophysical or instrumental effects also offer promising possibilities. Zandanel et al. (2015) for example suggests that the upcoming eROSITA survey (Merloni et al., 2012) will be able to distinguish dark matter decay by its behavior in an all-sky angular correlation analysis. Micro-calorimeters may also be able to detect the velocity shift and velocity broadening of X-ray spectral lines, which behave differently for dark matter decay or plasma emission due to the difference in dynamics between dark matter and gas, as described by Speckhard et al. (2016).

## **4.6 Appendix - Details of the Spectral Fits of Perseus with *Suzaku***

This appendix shows the additional details and figures of the fits for all of the *Suzaku* regions used in this work. Table 4.5 shows the best-fit parameters of the subregions 1a through 1c, while Figure 4.5 indicates graphically the best-fit gaussian line components for the best fit of Region 1.

Figures 4.6 and 4.7 show the spectra and residuals for all outskirts regions described in the text, being Regions 2, 3, 4, and 2-4.

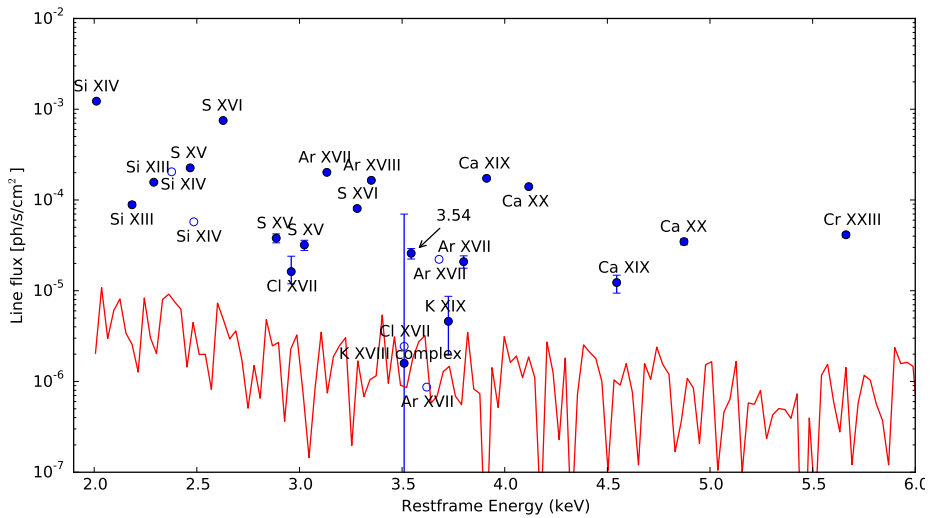


**Figure 4.5:** The gaussian line components of the best-fit model for Region 1, in units of  $\text{ph s}^{-1} \text{cm}^{-2}$ . Open circles indicate that the line flux was tied to another line in the fit. The red line indicates the residual level as the absolute value of the residuals in bins of 30 eV. Error bars are  $1\sigma$  obtained with the `error` command in `XSPEC`. Note that the two lines at  $\sim 3.51$  keV are the Cl XVII line which is tied to the line of the same ion at 2.96 keV, and the K XVIII complex whose maximum allowed flux is actually much lower than the formal error bar indicates (the maximum allowed flux is roughly  $2.4 \text{ ph s}^{-1} \text{cm}^{-2}$  as indicated by Tables 4.6 and 4.9 and in Section 4.2).

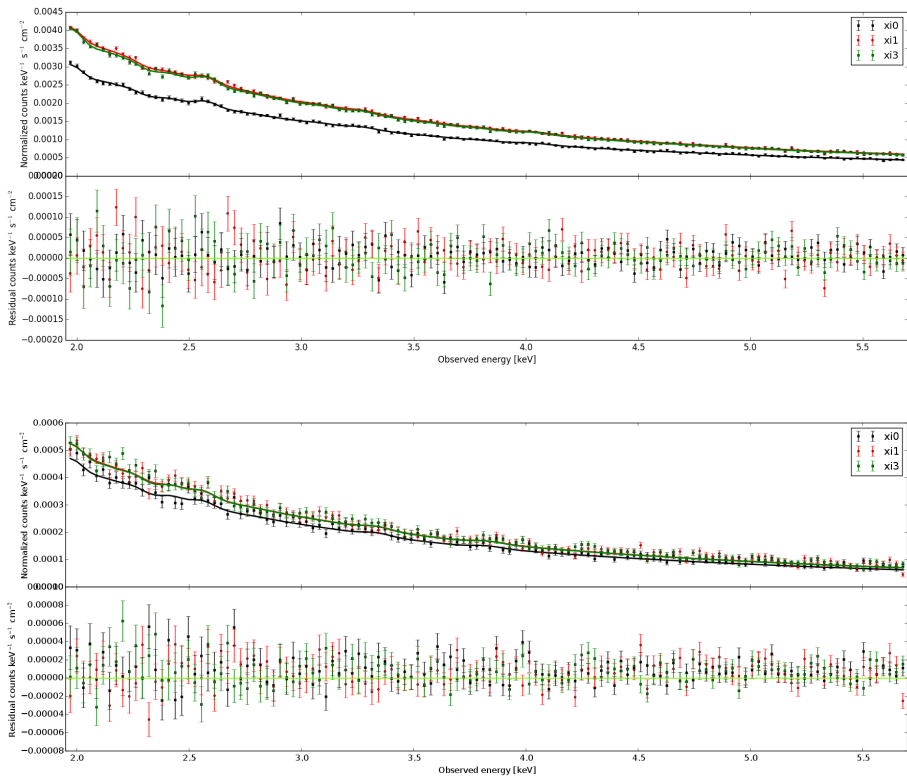


**Figure 4.6:** Regions 2 and 3. Showing the data and model fits to those regions, with the residuals in the bottom panel.

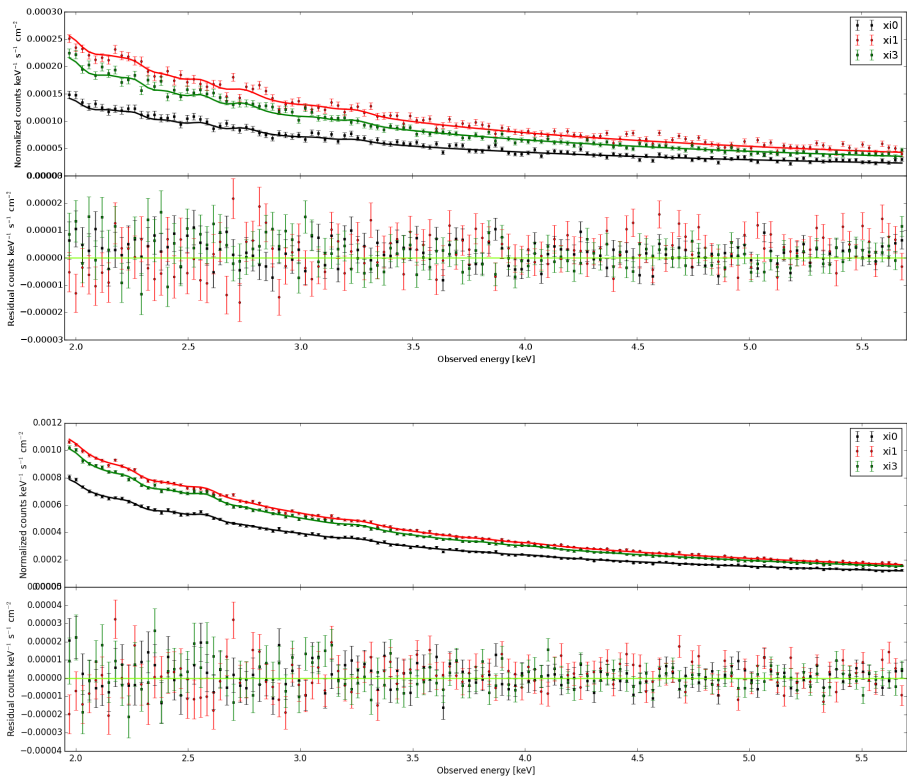


**Figure 4.7:** Regions 4 and 2-4. Showing the data and model fits to those regions, with the residuals in the bottom panel.

ObsID	FI	BI	$d$	ObsID	FI	BI	$d$	ObsID	FI	BI	$d$
	Exp (ks)	Exp (ks)	arcmin		Exp (ks)	Exp (ks)	arcmin		Exp (ks)	Exp (ks)	arcmin
101012020	79.9	39.9	0	804057010	24.1	12.0	32.80	806129010	12.9	6.4	75.36
102011010	70.2	35.1	0	806136010	13.1	6.5	32.81	804067010	43.9	22.0	81.63
102012010	107.0	53.5	0	805104010	13.9	6.9	32.88	806118010	27.1	13.6	81.79
103004010	68.2	34.1	0	806124010	19.1	9.5	33.11	806106010	24.7	12.4	82.67
103004020	92.6	46.3	0	801049040	15.0	7.5	33.12	805100010	18.9	9.5	82.82
104018010	33.9	17.0	0	801049010	50.3	25.2	35.94	805107010	15.2	7.6	83.11
104019010	67.2	33.6	0	806113010	19.1	9.5	40.25	804060010	43.2	21.7	83.15
105009010	59.2	29.6	0	806101010	19.5	9.7	40.86	806142010	31.6	15.8	83.23
105009020	66.0	33.0	0	806137010	21.0	10.5	41.23	806130010	27.5	13.7	83.55
106005010	68.2	34.1	0	806125010	11.1	5.6	41.72	808087010	34.8	17.4	87.97
106005020	68.5	41.1	0	804065010	24.5	12.2	48.03	806119010	32.5	16.3	90.56
107005010	66.4	33.2	0	806114010	16.3	8.2	48.21	805111010	13.1	6.5	91.08
107005020	60.5	35.6	0	805098010	13.5	6.7	49.02	806107010	30.4	15.2	91.42
108005010	62.5	38.1	0	806102010	14.4	7.2	49.05	805115010	19.5	9.7	91.53
108005020	68.2	34.1	0	804058010	22.8	11.5	49.58	806143010	19.6	9.8	91.60
804063010	26.9	13.5	14.48	806138010	19.7	9.9	49.59	806131010	27.9	13.9	92.00
806111010	21.6	10.8	14.70	805105010	21.8	10.9	49.61	804068010	60.2	30.1	98.38
805096010	16.3	8.1	15.54	806126010	15.0	7.5	49.93	806120010	17.1	8.6	98.57
806099010	23.1	11.6	15.58	806115010	23.8	11.9	56.99	805101010	29.5	14.7	99.48
807022010	46.0	23.0	15.78	806103010	20.5	10.3	57.79	806108010	20.6	10.3	99.49
807020010	46.0	23.0	16.01	806139010	17.5	8.8	58.08	804061010	56.8	28.4	99.92
804056010	14.2	7.1	16.01	806127010	20.4	10.2	58.39	805108010	24.9	12.4	99.95
805103010	12.9	6.4	16.07	701007020	71.4	35.7	59.21	806144010	20.6	10.3	100.05
806135010	18.6	9.3	16.16	701007010	6.8	3.4	64.34	806132010	13.9	7.0	100.37
807019010	27.4	13.7	16.22	804066010	42.9	21.5	64.87	806121010	14.1	7.1	107.34
806123010	19.7	9.8	16.44	806116010	21.7	10.8	65.11	805112010	26.2	13.1	107.82
805046010	35.2	17.6	16.62	806104010	26.4	13.2	65.96	806109010	13.7	6.9	108.17
805045010	53.5	26.8	17.91	805099010	18.6	9.3	65.97	805116010	24.9	12.8	108.29
805047010	33.4	16.7	18.76	806140010	12.6	6.3	66.32	806145010	25.5	12.7	108.32
807023010	27.1	13.6	19.10	804059010	36.6	18.3	66.40	806133010	16.2	8.1	108.99
807021010	35.8	17.9	19.13	805106010	19.9	9.9	66.53	804069010	60.8	30.4	115.20
805048010	29.1	14.5	19.13	806128010	20.4	10.2	66.90	806122010	20.7	10.3	115.46
801049030	61.0	30.5	27.74	806117010	20.4	10.2	73.79	806110010	20.7	10.4	116.21
801049020	53.7	26.9	31.21	805110010	18.0	9.0	74.38	805102010	25.8	12.9	116.24
806112010	21.7	10.8	31.37	806105010	17.3	8.6	74.60	804062010	54.5	27.4	116.70
804064010	19.1	9.6	31.44	806141010	22.2	11.1	74.79	805109010	30.7	15.3	116.74
806100010	18.0	9.0	32.26	805114010	13.7	6.9	74.82	806146010	14.6	7.3	117.04
805097010	21.2	10.5	32.47	808085010	37.4	18.7	74.85	806134010	22.0	11.0	117.10

**Table 4.8:** *Suzaku* observations of the Perseus cluster utilized in this study.  $d$  indicates the distance from the cluster center in arcminutes

Parameter	Reg 1	Reg 1a	Reg 1b	Reg 1c	Reg 2	Reg 3	Reg 4	Reg 2-4
kT based on S (keV)	3.13	2.97	3.18	3.25	3.74	2.37	2.47	3.60
kT based on Ca (keV)	4.02	3.65	3.92	4.85	4.77	–	–	4.14
Flux of Cl XVII at 2.96 keV	1571.18	882.46	868.90	415.20	50.52	5.52	2.19	11.00
Flux of Cl XVII at 3.51 keV	240.05	133.96	133.00	63.73	7.88	0.81	0.32	1.71
Flux of K XVIII at 3.47 keV	227.78	138.35	122.66	56.43	5.32	1.13	0.43	1.25
Flux of K XVIII at 3.49 keV	112.44	68.27	60.59	27.90	2.65	0.57	0.22	0.62
Flux of K XVIII at 3.51 keV	471.09	280.16	255.33	118.56	11.78	2.13	0.82	2.73
Flux of Ar DR XVII at 3.62 keV	66.87	44.72	35.00	15.46	1.14	0.58	0.20	0.29

**Table 4.9:** Same as Table 4.6 but for Anders & Grevesse (1989) solar abundances: sstimated fluxes of the Cl XVII, K XVIII, Ar DR XVII lines are in the units of  $10^{-8}$  phr  $\text{cm}^{-2}$   $\text{s}^{-1}$  from AtomDB. The fluxes (and not the temperature) in this table are dependent on the assumed solar abundance, and are employed in the fits by setting the upper and lower allowed limits for the fitting procedure to 3 times and 0.1 times this flux, respectively.

